Laboratory Apparatus and Cumulative Damage Model for Linking Field and Laboratory Exposure Results

by

Jonathan W. Martin, Tinh Nguyen, Eric Byrd, Brian Dickens and Ned Embree
Building and Fire Research Laboratory
National Institute of Standards and Technology
Gaithersburg, MD 20899 USA

Reprinted from the Service Life Prediction: Methodology and Metrologies, American Chemical Society Symposium Series 805, Jonathan W. Martin, David R. Bauer, eds., pp. 119-143, 2002.

NOTE: This paper is a contribution of the National Institute of Standards and Technology and is not subject to copyright.

NIST
National Institute of Standards and Technology
Technology Administration, U.S. Department of Commerce

Chapter 7

Laboratory Apparatus and Cumulative Damage Model for Linking Field and Laboratory Exposure Results

Jonathan W. Martin, Tinh Nguyen, Eric Byrd, Brian Dickens, and Ned Embree

National Institute of Standards and Technology, 100 Bureau Drive, Stop 8621, Gaithersburg, MD 20899-8621

A laboratory apparatus and a cumulative damage model are described for linking field and laboratory photodegradation results for polymeric materials. The apparatus is capable of independently and precisely controlling or monitoring the three primary weathering factors in both space and time. These factors are temperature, relative humidity, and spectral ultraviolet radiation. Linkage between field and laboratory results will be made through measurements of dose, dosage, and material damage. These measurements are input into the model to estimate the apparent spectral quantum yield and the total effective dosage for a model acrylic melamine coating. The model coating was exposed at twelve different spectral wavebands over a wide range of temperatures and relative humidities. Variables affecting the accuracy of the measurements are discussed.

Introduction

This paper describes a laboratory apparatus and a cumulative damage model, called the total effective dosage model, for use in linking field and laboratory photodegradation results for polymeric materials. This model has gained widespread acceptance in medical and biological studies since the mid-1900s (1,2). The total effective dosage model has a firm basis in the principles of photochemistry, including the Lambert-Beer law, the photochemical law, the reciprocity law and the spectral-independence-of-damage assumption, often called the law of additivity (3). This model differs from generally accepted field exposure metrics such as total exposure

© 2002 American Chemical Society

time (4), total solar irradiance (5,6) and total-UV irradiance (7) in that the spectrum of incident radiation is broken up into regions, each of which is treated independently and each region is weighted as to its photolytic effectiveness. For most polymeric materials, quanta at wavelengths of solar ultraviolet closer to 290 nm tend to have a higher photolytic efficiency than do quanta at longer wavelengths. Broadband exposure metrics like total solar irradiance and total-UV irradiance assume that the photolytic effectiveness of all quanta in the radiant spectrum is constant.

Total Effective Dosage Model

The number of photons absorbed by a material, the dosage, is given by

$$D_{dosage}(t) = \int_0^t \int_{\lambda_{min}}^{\lambda_{max}} E_o(\lambda,t)\left(1-10^{A(\lambda,t)}\right) d\lambda \, dt$$

[1]

where

λ_{min} and λ_{max} = minimum and maximum photolytically effective UV-visible wavelengths (units: nm),

A (λ,t) = absorbance of sample at specified UV-visible wavelength and at time t, (units: dimensionless) [note, for polymers containing UV stabilizers or absorbers the absorbance term can be partitioned to account for the spectral absorbance from each component],

$E_o(\lambda,t)$ = incident spectral UV-visible radiation dose to which a polymeric material is exposed to at time t (units: J cm^{-2}),

= elapsed time (units: s).

The total effective dosage, D_{total}, is the total number of absorbed photons that effectively contribute to the photodegradation of a material during an exposure period. It has the form

$$D_{total}(t) = \int_0^t \int_{\lambda_{min}}^{\lambda_{max}} E_o(\lambda, t)\left(1-10^{-A(\lambda,t)}\right)\phi(\lambda) \, d\lambda \, dt$$

[2]

where

$D_{total}(t)$ = Total effective dosage (units: J cm^{-2}) and

ϕ (λ) = spectral quantum yield, the damage at wavelength λ relative to a reference wavelength (dimensionless).

Photolytic damage to a polymeric material has been empirically related to dosage, D_{dosage}, by a damage function. Commonly published damage functions include a linear response

$$\Gamma = a\, D_{dosage}$$

a power law response

$$\Gamma = a\, (D_{dosage})^{b}$$

and an exponential response

$$\Gamma = a \exp(b\, D_{dosage})$$

where a and b are empirical constants and where damage is any quantitative, performance characteristic that is considered to be critical to a material's field performance.

The apparent quantum yield, $\phi(\lambda)$, in Equation 2 is estimated from the initial slope of the material damage, Γ, versus dosage, $D_{dosage}(t)$, curve for a material exposed at wavelength λ. Once the apparent spectral quantum yield has been estimated, then this value can be substituted back into Equation 2 after which the total effective dosage, D_{total}, can be determined. Although this can be accomplished, the estimated total effective dosage are only realistic when the damage versus dosage curves are linear.

Experiment

Materials and Specimen Preparation:

Coating

Bauer, Gerlock and others (8,9) have extensively studied the photochemistry of the model acrylic melamine coating selected for this study. The coating is made from a mixture of a hydroxy-terminated acrylic polymer and a partially-alkylolated amine crosslinking agent in a mass ratio of 70:30. The acrylic polymer contains 68% by mass normal butylmethacrylate, 30% hydroxy ethylacrylate, and 2% acrylic acid and is supplied as a mixture 75% by mass acrylic polymer and 25% 2-heptanone. The crosslinking agent used is Cytex Industries Cymel 325[1], which is a mixture containing 80% by mass melamine formaldehyde resin and 20% isobutanol solvent. The glass transition temperature of the cured coating as determined by dynamic mechanical analysis was 45° C ± 3° C for our material.

Calcium fluoride (CaF_2) disks having dimensions of 100 mm diameter and 9 mm thick were selected for the laboratory substrates. CaF_2 is transparent for wavelengths between 0.13 μm to 11.5 μm (10). For the field exposure experiments, silicon and quartz substrates were selected due to the high cost of the CaF_2 disks. Silicon is transparent for wavelengths between 1.2 μm to 15 μm and is a good substrate for studying photodegradation via FTIR analysis in the transmission mode. Quartz is transparent from 0.12 μm to 4.5 μm and, therefore, it is a suitable substrate for

studying changes in spectral UV absorbance. All three substrates have excellent moisture and temperature resistances.

Solutions of acrylic polymer and melamine crosslinking agent were mixed at the manufacturer's suggested ratio, degassed, spread onto the substrates, and spin cast at 2000 rpm for 30 seconds. The coatings were then cured at 130 °C for 20 minutes. This schedule completely cured the coatings as verified by Fourier transform infrared spectroscopy (FTIR). The average and standard deviation of the cured coating thicknesses were 10.4 μm ± 0.5 μm as estimated by a prism coupling technique (11).

Apparatus

Solar Simulators

Two Oriel Instruments solar simulators[1] were procured for this study. A schematic of the simulator is shown in Figure 1. Each solar simulator's optical system included a 1000 W xenon arc lamp, a parabolic mirror, a dichroic mirror, an optical integrator, a cold mirror, a 36 cm diameter Fresnel collimating lens, and a light intensity controller (not shown in Figure 1).

Ultraviolet radiation emitted from the xenon arc is reflected from the parabolic mirror to the dichroic mirror. Visible and infrared portions of the xenon arc spectrum pass through the dichroic mirror and are absorbed by a heat sink. The ultraviolet portion of the xenon arc spectrum is reflected off the dichroic mirror through the optical integrator. The optical integrator homogenizes the beam and the Fresnel lens collimates the beam. For our setup, the heat-induced irradiance of the specimens was less than 2° C above the ambient temperature.

Exposure Cells

The laboratory exposure cells were designed to simultaneously expose different sections of the same film to 12 well-defined, spectral radiation bandwidths. A complete description of the exposure cell and the exposure cell arrangement under the two solar simulators has been given in Reference 11. This section briefly describes the design of an exposure cell and the arrangement of the solar cells under each solar simulator.

The exposure cells were arranged as shown in Figure 2. Exposure cells 1 through 4 were irradiated under the left-hand solar simulator while exposure cells 5 through 8 were irradiated under the right-hand solar simulator.

---

1 Certain commercial instruments and materials are identified in this paper to adequately describe the experimental procedure. In no case does such identification imply recommendation or endorsement by the National Institute of Standards and Technology nor does it imply that the instrument or materials are necessarily the best available for the purpose.

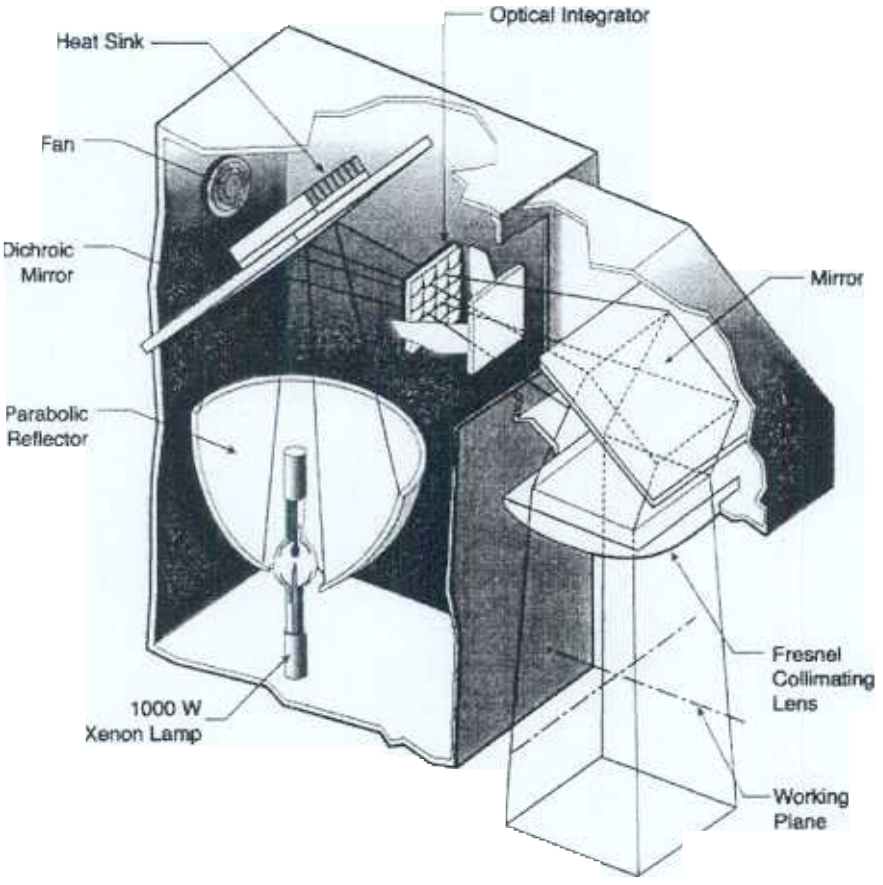

Figure 1. Schematic of solar simulator showing the arrangement of its optimal components.

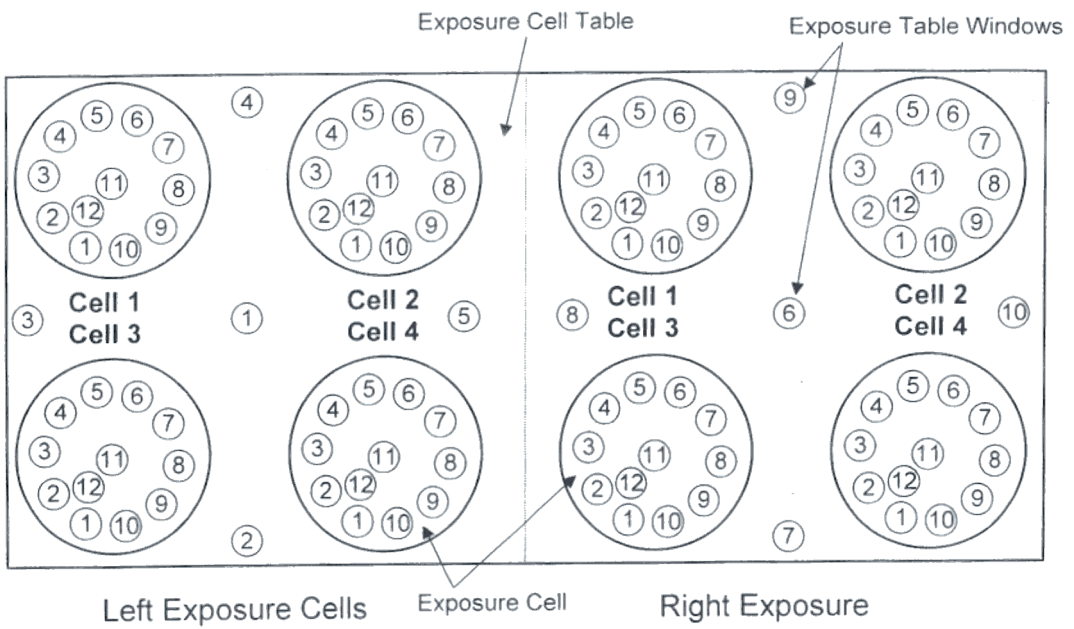

Figure 2. Arrangement of the eight exposure cells on the exposure table and the arrangement of the 12 windows within each exposure cell. The 12th window is only in the specimen disk and is used in studying non-photolytic degradation.

A cross sectional schematic of an exposure cell is shown in Figure 3. Each exposure cell has a layered design that included a filter disk, a quartz disk, a CaF_2 specimen disk and an encasement to hold the disks. The filter disk contained 11 windows: 10 on the disk perimeter and the 11th in center (the 12th window is displayed in Figure 2, but this window was only open in the specimen disk). Each window is 16 mm in diameter. A slot machined into the top of each window supports an interference filter and the bottom is beveled with a knife-edge to minimize grazing angle reflections from the interior sides of the window.

Each of the 10 perimeter windows was outfitted with a narrow bandwidth interference filter covering a different segment of xenon arc radiant spectrum from 290 nm to 550 nm. Nominally identical interference filters were used in all eight-exposure cells. The first eight interference filters had full-width-half-maximum (FWHM) values between 2 nm and 10 nm and covered the range between 290 nm and 340 nm. The nominal center wavelengths for these filters were 290 nm, 294 nm, 300 nm, 306 nm, 312 nm, 318 nm, 326 nm, and 336 nm. The two remaining filters had FWHM values greater than 10 nm and had center wavelengths of 354 nm and 450 nm. The 290-nm center wavelength interference filter was selected because 290 nm is the lowest radiation reaching the Earth's surface (12). The center wavelengths were selected to cover the range of suspected photolytic activity. The FWHM for each filter was selected in an effort to degrade the coating at the same rate. This selection process was based on three a priori assumptions: 1) the photolytic effectiveness (i.e., spectral quantum yield) monotonically decreases with increasing wavelength; 2) between 290 nm and 500 nm the apparent spectral quantum yield decreases by approximately three orders of magnitude (13); and 3) the spectral output of the xenon arc lamp approximates the solar radiant flux.

The center window (i.e., the 11th window) was termed the "full UV-radiation" window because, in the first study, it was not outfitted with a filter and, thus, transmitted all of the spectral radiant flux emitted from the solar simulator. In subsequent studies, a short pass filter (Schott filter KG-1, KG-2, KG-3, or KG-5) was inserted into this window to remove radiation below 290 nm.

The CaF_2 specimen disk was sandwiched between two aluminum plates (see Figure 3). Each plate contained 12 windows. The aluminum plates protected the CaF_2 from damage during handling while the windows allowed a portion of the film to be exposed to a specific wavelength treatment. The top aluminum plate was positioned about 1 mm above the coating while the bottom plate was in direct contact with the lower surface of the CaF_2 disk. All 12 windows in the top and bottom plates had the same dimensions and so aligned that radiation could exit the exposure cell without back reflection. The $12^{th\ window}$ was termed the "no-UV" or "dark window" and was used in assessing non-photolytically induced degradation.

The exposure cell was machined to tight tolerances so that a small positive pressure could be maintained within the exposure cell chamber. The quartz disk acted as the top of the exposure cell chamber and protected the interference filters from the degrading effects of moisture while transmitting essentially the entire incident UV radiation. The CaF_2 disk acted as the bottom of the chamber while the encasement acted as the sides.

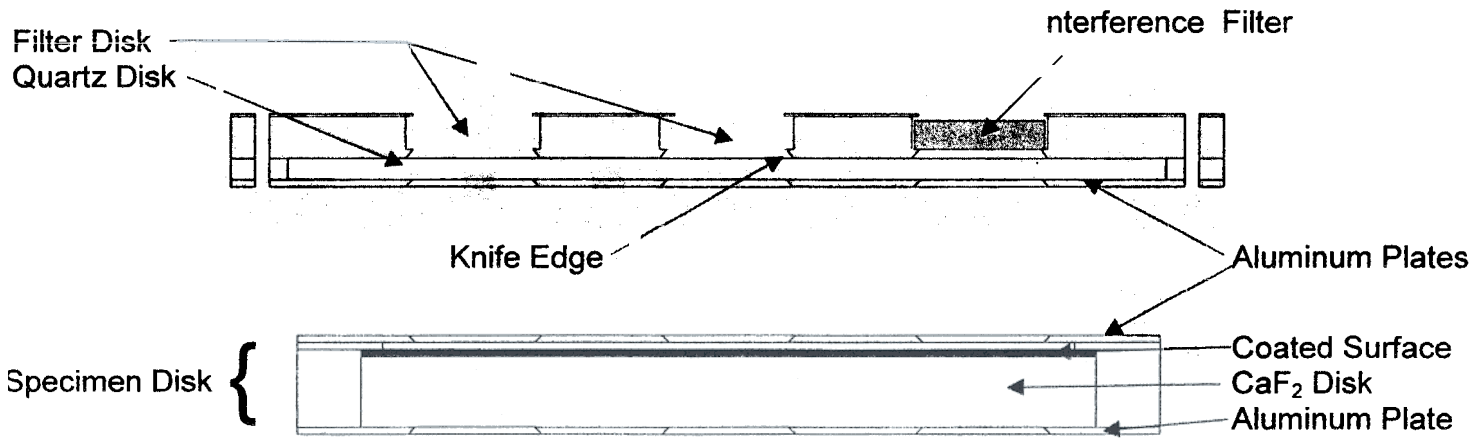

Figure 3. Exploded cross sectional view of an exposure cell showing the arrangement of interference filters and the quartz and the coated CaF_2 disks.

igure *ontinued.*

Inlet and outlet ports were drilled into the exposure cell chamber letting air having a specified temperature and relative humidity (RH) in and out of the chamber. The conditioned air was generated in a humidity-temperature generator and pumped into each exposure cell. The temperature within the exposure chamber was monitored via a thermocouple positioned inside the chamber. The RH of the air flowing into the exposure cells was monitored by rerouting a portion of the air flowing into the chamber through a chilled mirror hygrometer for five minutes out of every 20 minutes. Temperature and RH measurements within each exposure cell were made on a continuous basis throughout the duration of the experiment.

Humidity-Temperature Generators

Two identical temperature-humidity generators were designed and fabricated to provide air of known RH and temperature to the four exposure cells positioned under each solar simulator. Each temperature-humidity generator was capable of providing conditioned air at one temperature and up to four different relative humidities. The RH of the air pumped into each exposure cell could be independently controlled and maintained to within ± 3% between 0% and 95% RH; while the temperature could be maintained at any value from a few degrees Celsius above room temperature to 70° C ± 1° C.

Measurements:

UV-Visible and Infrared Transmittance Measurements

Dosage, D_{dosage}, not time or dose, is the exposure metric used in these experiments. Dosage is the total number of photons absorbed by a pure material whereas the dose is the number of incident photons. To accurately estimate the dose and dosage, the optical properties of all of the components identified in Figures 4 had to be measured and account taken of 1) the spatial, temporal and spectral variability in the radiant flux of the light source and 2) the spectral transmittances of the interference filters, quartz plate, and coated CaF_2 disks for all eight exposure cells. These measurements were made prior to the start of the experiment and at every inspection period.

Measurements of the optical properties of the system components were highly automated (11). Automation was achieved through three devices: 1) a robotic arm connected to a HP 8452A UV-visible spectrophotometer via a fiber optic cable, 2) a 150 mm diameter PIKE automated ring inspection device inserted into the optical beam path of the HP 8452A UV-visible spectrophotometer, and 3) a second 150 mm diameter PIKE automated ring inspection device inserted into the optical beam path of a Perkin Elmer 1760X FTIR spectrophotometer.

The HP 8452A spectrophotometer was calibrated against NIST's standard reference xenon arc lamp at least twice a year. This calibration curve allowed the

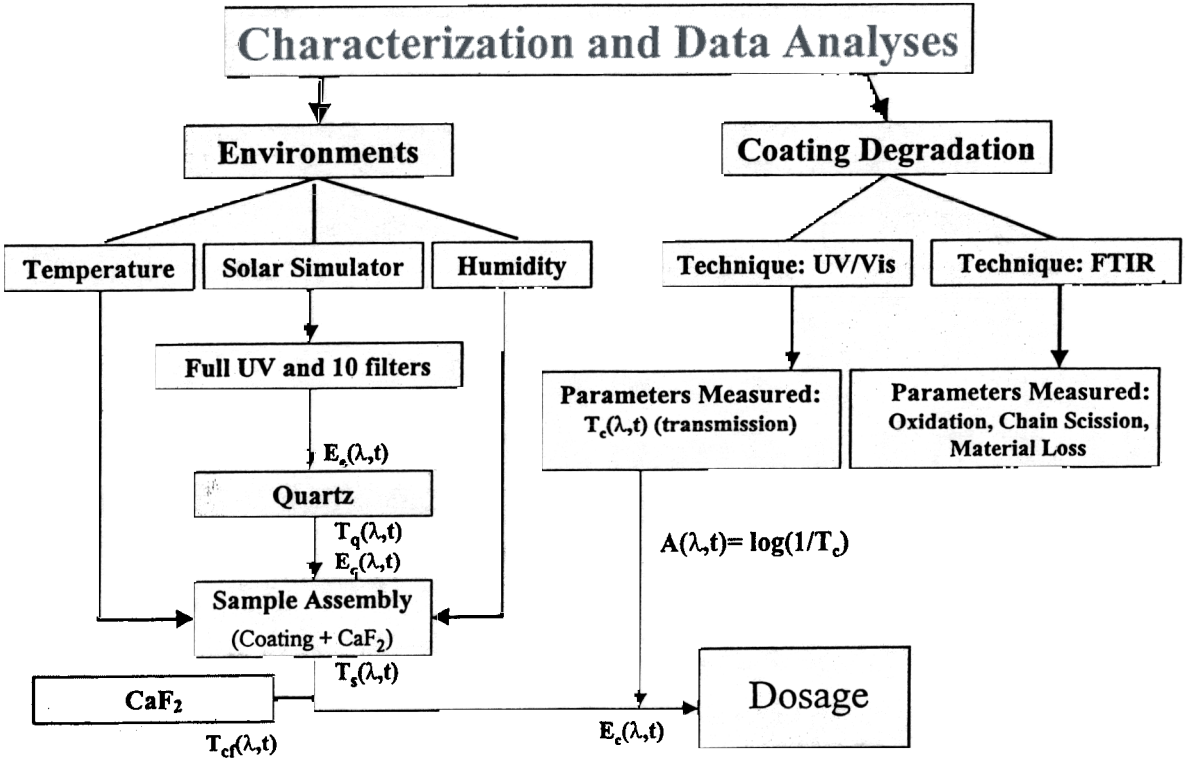

Figure 4. A flowchart displaying the various measurements for making dosage and damage assessments during each inspection.

conversion of the UV-visible signal into photon counts. About midway through the experiments, it became apparent that even a small imprecision in the spectral UV measurements could greatly affect the estimated dosage. To improve the accuracy of these measurements, the UV-visible spectrometer was recalibrated during each inspection against standard UV-visible spectrometer transmittance density filters using NIST Standard Reference Material (SRM 930d) while the FTIR spectrometer was calibrated using a 38.1 μm thick polystyrene film.

Dosage and Apparent Spectral Quantum Yield Calculation Computer Program

A software program [14] was written to estimate dose, dosage, and material damage given the input from the optical components shown in Figure 4. That is, dose and dosage were estimated from the UV-visible spectra of the lamps, the transmittances of the interference filters, quartz disk, and coated CaF_2 disks and from the UV-visible absorbance of the coating specimens. Some of the optical values changed with time. For example, the spectral radiant flux emitted by the xenon arc lamp changed non-uniformly with time as the light source aged, even though the light source was equipped with a light intensity controller. The experimental procedure involved monitoring changes in UV-visible spectra during each inspection. Once the output of the lamp and the transmittance of the interference filters, quartz disk, and coated CaF_2 disk were known, the spectral dose incident on a specimen could be estimated. Knowing the absorbance of the uncoated and coated calcium fluoride disk, the transmittance of the specimen could be determined. Radiant energy incident on the specimen that did not emerge from the other side of the specimen was presumed to have been absorbed by the specimen and was used in estimating dosage. Besides calculating spectral dose and dosage, the software package is capable of analyzing infrared spectra, plotting the damage function, estimating the apparent spectral quantum yield, and estimating the total effective dosage.

Experimental Design:

Specimens were exposed to 16 combinations of temperature and RH at each of 12 different spectral bandwidths. The nominal RH's were 20%, 40%, 70% and 90% while the nominal temperatures were 30° C, 40° C, 50° C, and 60° C. An additional experiment was conducted at 50° C and at RH close to 0%.

All eight exposure cells were simultaneously irradiated. The four exposure cells exposed under the right solar simulator (designed the right exposure in Figure 2) were held at a different temperature than the exposure cells exposed under the left solar simulator. The temperatures usually differed by 10° C. The temperature of each set of four exposure cells irradiated under the same simulator was maintained at approximately 1° C to 2° C above the specified exposure cell temperature. This was achieved by surrounding the exposure cells with 8 mm thick poly (methyl methacrylate) walls and heating the interior space. Increasing the temperature around

the exposure cells was necessary to prevent the formation of condensation of water on the top surface of the coating within an exposure cell for the high humidity exposures.

Results and Discussion

Environmental Characterization

Spatial Uniformity, Collimation and Temporal Stability of UV-Visible Light Source

Results on the spatial uniformity, collimation, and temporal stability of the UV-visible light source have been graphically and tabularly presented in Reference 11. In general, the spectral radiant flux differed from one solar simulator to another and differed from one lamp to another.

One example is displayed in Figures 5a and 5b for the spatial radiant flux distributions at 380 nm of the right and left solar simulators. The mean and standard deviation for radiant fluxes at 380 nm for the two solar simulators were 0.13 $W/m^2 \pm 0.014$ W/m^2 and 0.19 $W/m^2 \pm 0.026$ W/m^2, respectively. The radiant flux from the right solar simulator was always 50 % less than the radiant flux from the left simulator; even when the same xenon arc source was used in both simulators. These spatial irradiance differences were measured at 110 locations under the two simulators at each inspection time using the robotic arm positioned underneath the exposure cell table. This data was used in the dose and dosage software program to calculate the incident radiation at every window for each exposure cell.

The spectral radiant flux of the xenon arc light sources also changed non-uniformly with time. For example, after 1500 h of lamp operation, the spectral radiant flux decreased with respect to initial values at 290 nm, 326 nm and 450 nm by 25%, 50%, and 38%, respectively. These changes demonstrate the need for frequent monitoring of the spectral radiant flux emitted by the light source.

Beam collimation and scattering of the radiation were measured in both solar simulators. Measurements using the fiber optic probe positioned at the end of the robotic arm and connected to the UV-visible spectrometer. The degree of collimation was ascertained by measuring the radiant flux below the center points of several randomly selected windows. Measurements were made while displacing the fiber optic probe in 10 mm increments until the sensor was 100 mm from the initial position. Radiant flux measurements were plotted against vertical distance and regression analysis was performed. The slope of the regression curve was not significantly different from zero suggesting that the radiant output from each solar simulator was highly collimated. The absence of stray light incident on the covered

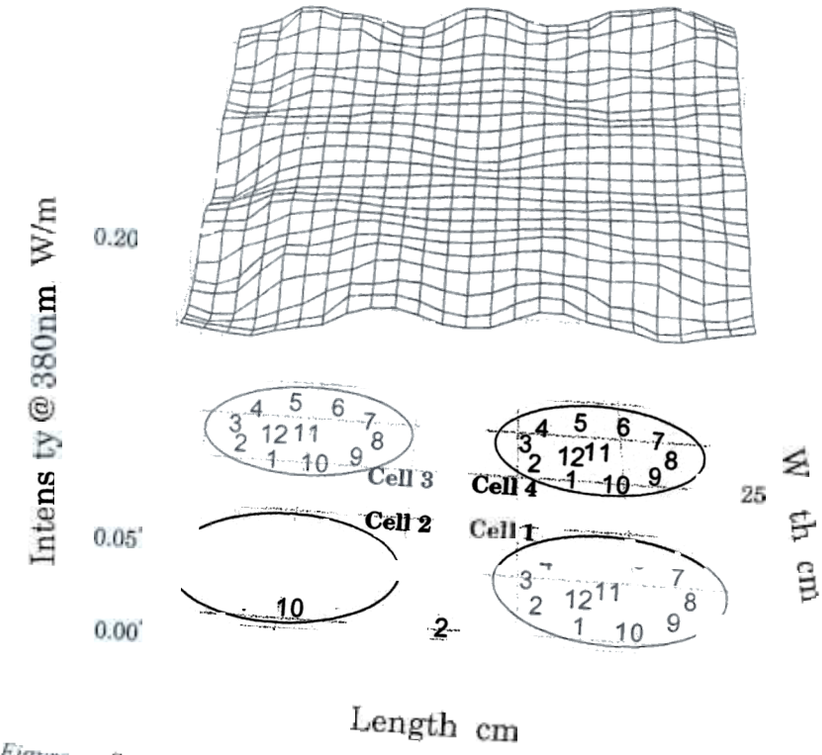

Figure Spatial irradiance uniformity of right and left solar simulators

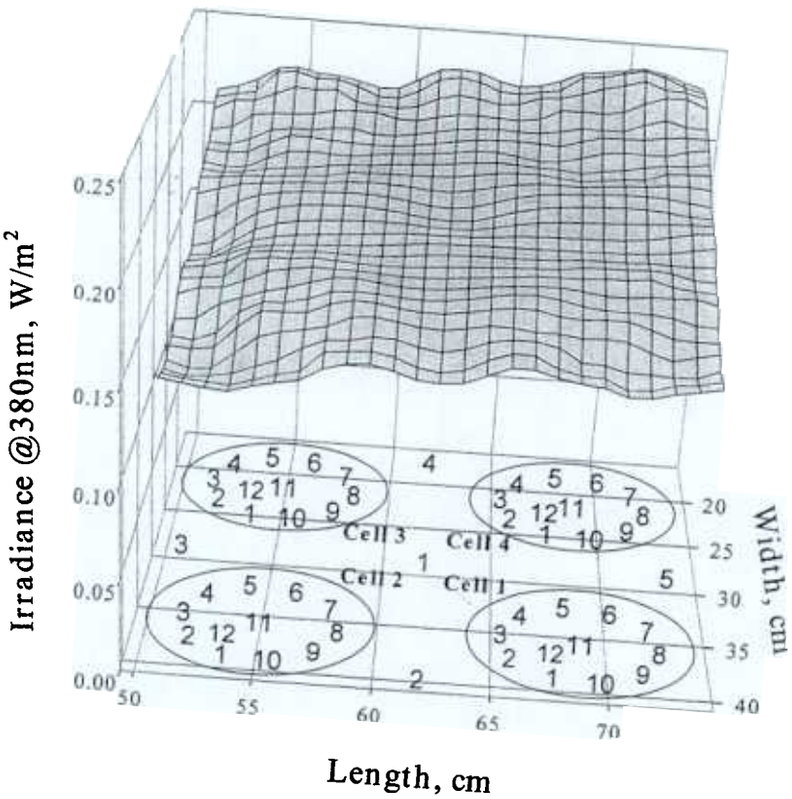

Figure 5. *Continued*

12th window was verified by positioning the fiber optic probe immediately beneath this window. No UV-visible radiation was detected.

Temporal Stability of Interference Filters, Quartz Disk and Calcium Fluoride Disk

The CaF_2 did not exhibit any loss of transmission over time. The interference filters were also photolytically and thermally stable except for the 450-nm filter; the loss of transmission for this filter ranged from 2% to 7% after six months of exposure. The quartz plates showed a small transmission loss over the course of exposure. All of these changes were accounted for in the software program used for calculating dose and dosage.

Temporal Control of Temperature and Relative Humidity Within the Exposure Cells

Both temperatures and relative humidities were well controlled. The standard deviations of the four RH levels studied (20 %, 40 %, 70 % and 90 %) ranged between 3 % and 7 % and the standard deviations of the four temperatures (30 °C, 40 °C, 50 °C, and 60 °C) ranged between 0.4° C to 1° C (11). With further refinement of the temperature-humidity generators, relative humidity was controllable to within ± 2%.

Coating Degradation

Photodegradation results for the acrylic melamine coating are presented in this section to demonstrate the approach for measuring material damage and calculating dosage. Figure 6a and 6b show FTIR spectra of the coating before and after aging for 2040 h under full UV at 50° C and close to 0 % RH, and Figure 6c is the difference spectrum between the aged and unaged samples. The major FTIR bands of interest in the cured, unaged acrylic melamine coating are the absorptions near 3530 cm^{-1}, due to OH stretching of the acrylic resin, near 3380 cm^{-1}, due to OH/NH stretching of the melamine resin (15), and at 1085 cm^{-1} and 1015 cm^{-1}, due to C-O stretching. The band near 1555 cm^{-1} has been assigned to the contribution of three different groups: triazine ring, CN, and CH_2 (16). Although not visible in Figure 6a, two important bands that are frequently used for curing and degradation analyses of melamine-based coatings are the bands at 910 cm^{-1} (OCH_3) and at 815 cm^{-1} (the triazine ring out-of-plane deformation). From Figure 6a, the cured film still contained a substantial amount of unreacted OH groups of the acrylic resin, and unreacted methylol or imino and OCH_3 groups of the melamine crosslinking agent. The presence of these groups in the cured films can affect both the photolysis and hydrolysis of acrylic melamine coatings (9,17,18).

The difference spectrum given in Figure 6c indicates that the coating has substantially degraded after 2040 h exposure. This is evidenced by the decreases in intensity in the 2750 cm^{-1} - 3050 cm^{-1} and 1600 - 1000 cm^{-1} regions and increases in the intensity in the 3100 cm^{-1} - 3400

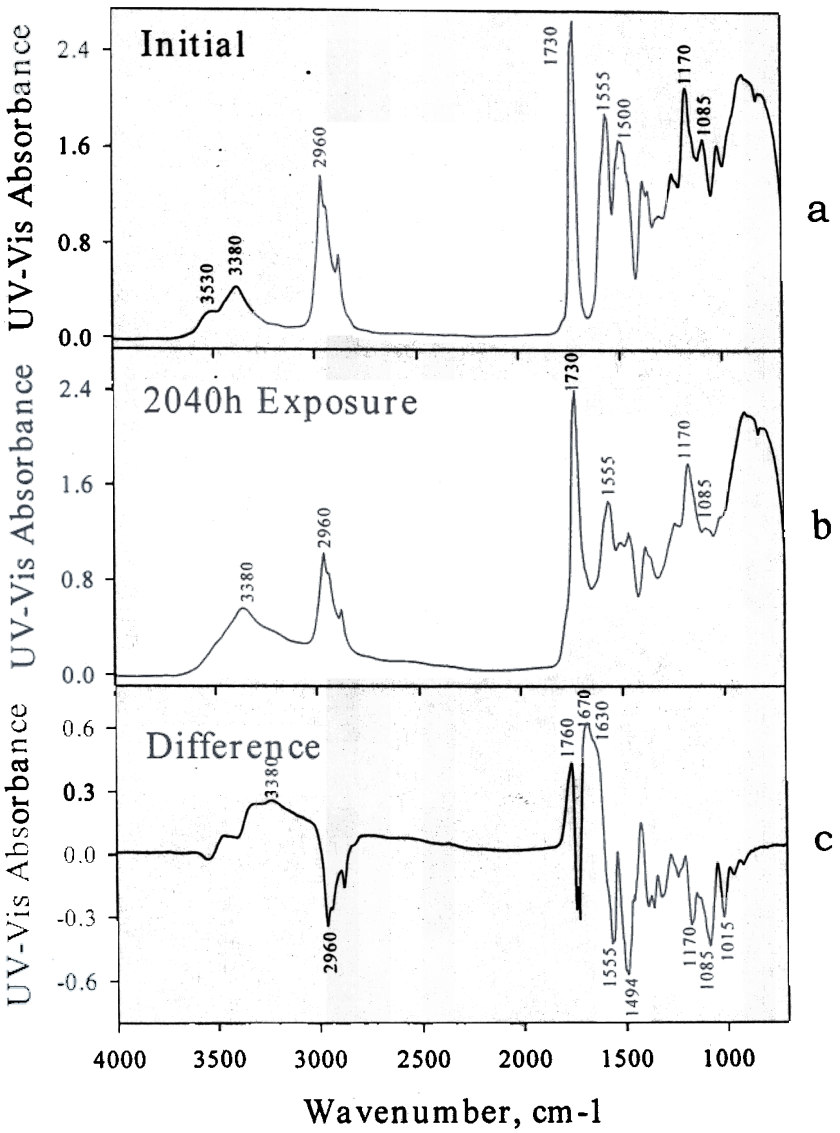

Figure 6. FTIR spectra of acrylic melamine coating (a) unaged, (b) after exposure for 2040 h in full UV, 50° C and close to 0% RH, and (c) difference spectrum (b minus a).

cm^{-1} regions and of the bands near 1760 cm^{-1}, 1670 cm^{-1}, and 1630 cm^{-1}. Analysis of amide model compounds and D_2O treatment of the UV-degraded specimens suggest that the band at 1670

cm^{-1} is due to the C=O of an amide and that.the band at 1630 cm^{-1} is due to the NH bending of primary amines or primary amides. These assignments are consistent with Lemaire's scheme of photodegradation for acrylic melamine coatings (19) and with literature assignments of functional groups of amine and amide compounds (20). Complete assignments of the cured coating before and after exposure to the environments are given in Reference 18.

In this study, we used the amide C=O band at 1670 cm^{-1} and the C-O band at 1085 cm^{-1} to follow the oxidation and crosslink chain scission, respectively. Bauer and coworkers have utilized the integrated area in the 1550 cm^{-1} - 1750 cm^{-1} region (8), and later the intensity of the 1630 cm^{-1} band (9), to follow the photo-oxidation of acrylic melamine coatings exposed to UV conditions. Figures 7a and 7b depict FTIR intensity changes of the 1670 cm^{-1} and 1085 cm^{-1} bands, respectively, as a function of time for different spectral UV-visible conditions at 50° C and 0% RH. The changes in these band intensities were due to photolysis because post-curing effects have been removed. The photodegradation of this coating exposed to the full UV condition (inset) was much greater than that of any of the ten filters. Under full UV, the rates of both photo-oxidation and crosslink chain scission were almost constant with exposure time after an initial slow down. Further, under these exposure conditions, nearly 25 % of the C-O groups were lost after three months of exposure.

Total Effective Dosage and Apparent Spectral Quantum Yield

Figures 8a and 8b display photo-oxidation (1670 cm^{-1}) and crosslink chain scission

(1085 cm^{-1}) as a function of dosage for specimens exposed to full UV, several filters and at 50 °C and close to 0 %RH. The dosage was calculated using Equation 1. Specimens exposed under the 294 nm, 300 nm, and 306 nm filters exhibited the least damage per unit dosage while specimens exposed under the 326 nm filter exhibited the greatest damage per unit dosage, despite the fact that the highest dosage was recorded at the 354 nm filter.

The apparent spectral quantum yield is taken as the initial slope of the damage/dosage curve. The use of this initial slope avoids complications from multiple degradation processes and from potential shielding of the coating material by degradation products absorbing radiation. In the process of determining this slope, a fourth-order polynomial function was fitted to the damage/dosage curve. In this first implementation of analyzing this curve, the slope at the 10 % of the dosage was used as the point at which to estimate the apparent quantum yield. One example of such fitting is shown in Figure 9 for the 1085 cm^{-1} and 1670 cm^{-1} bands, where the symbols are the experimental data and the solid lines are the fitted curves. The initial part of the damage/dosage curves at 1085 cm^{-1} exhibits considerable scatter due to

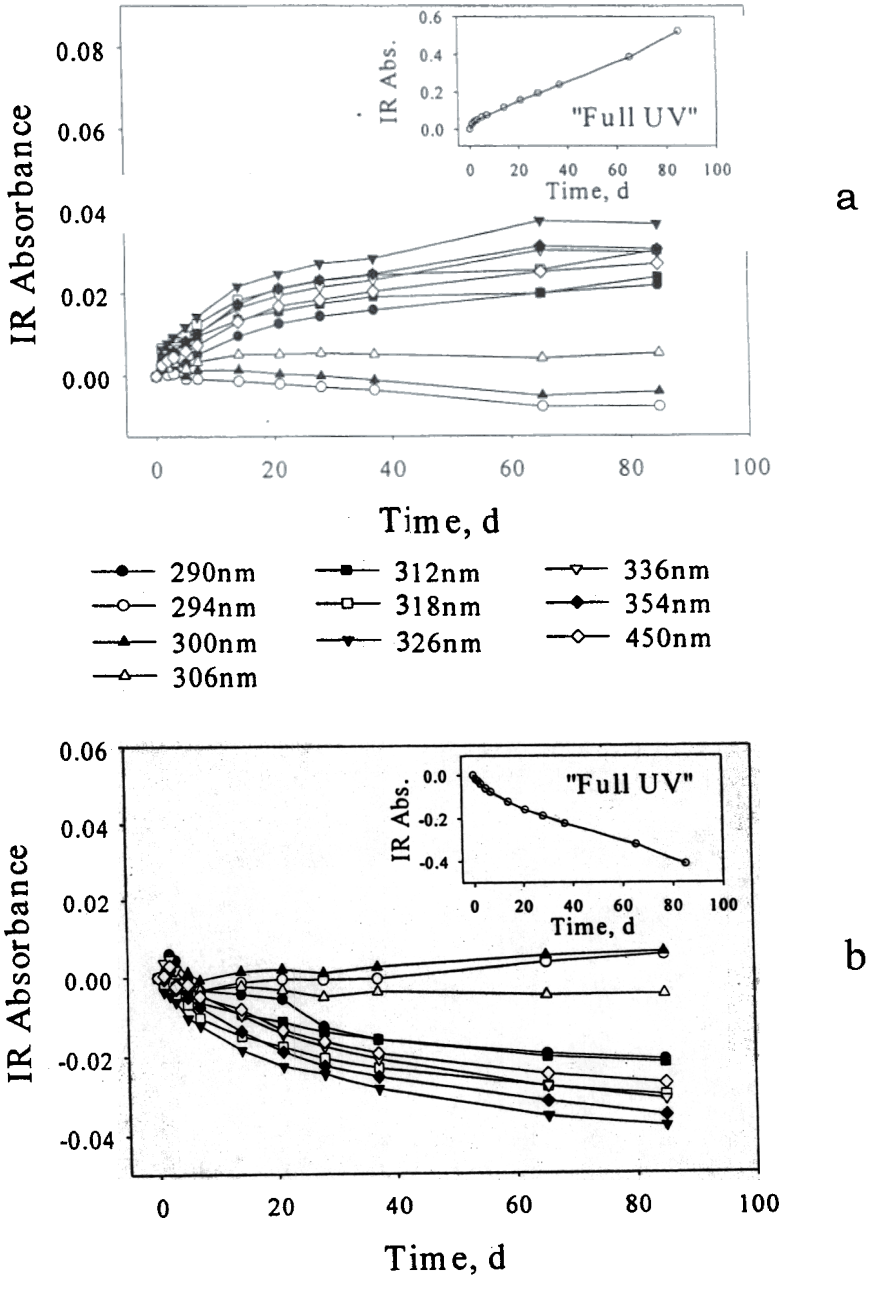

Figure 7. FTIR intensity changes of the bands at 1670 cm^{-1} (a) and at 1085 cm^{-1} (b) versus exposure time. Exposure conditions were 50° C and close to 0% RH.

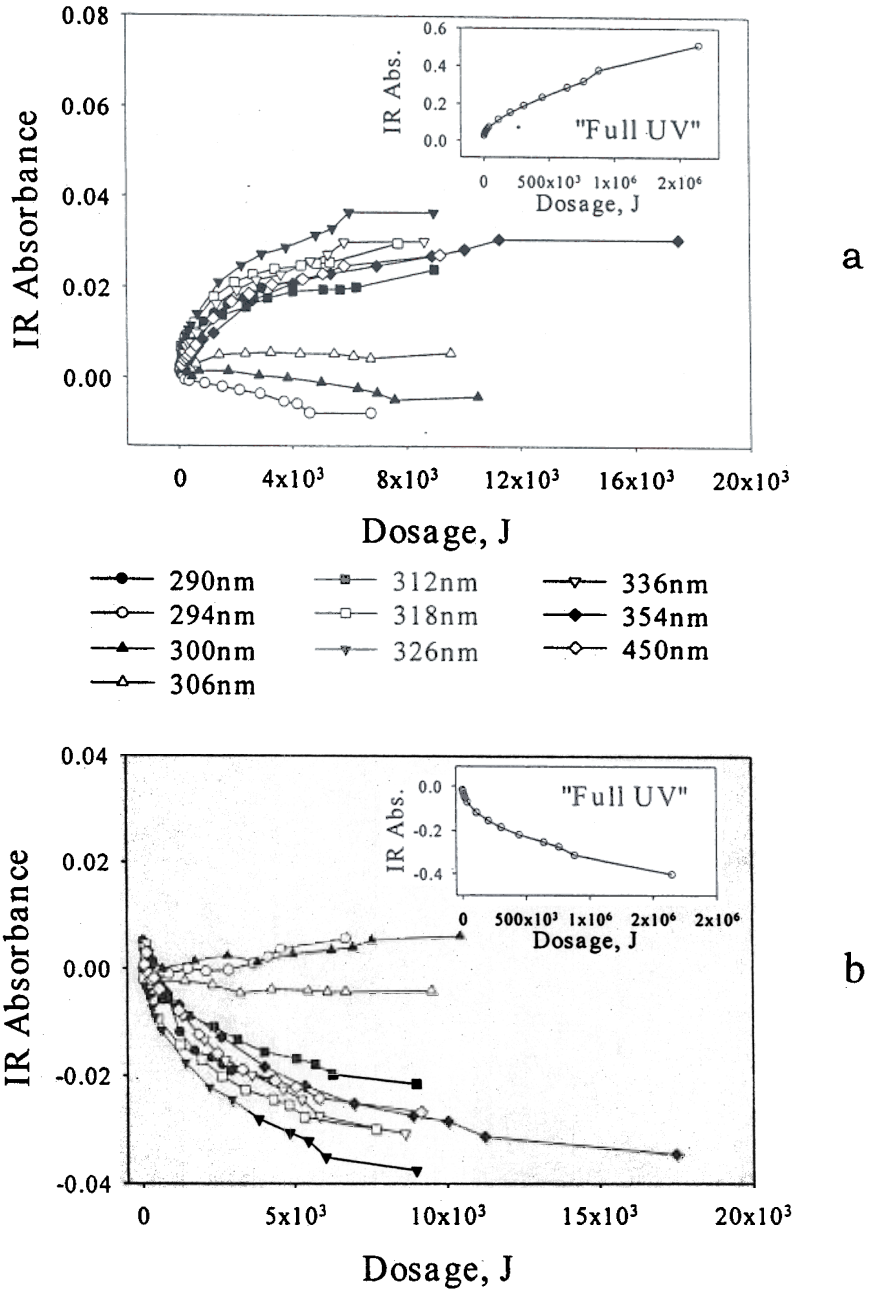

Figure 8. Oxidation (a) and crosslink chain scission (b) as a function of dosage for an acrylic melamine coating exposed to 50° C and close to 0% RH to full UV and under the 10 interference filters.

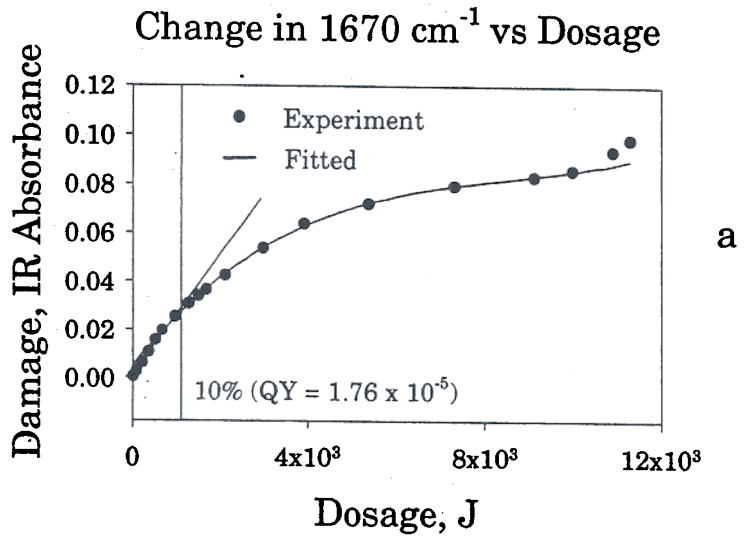

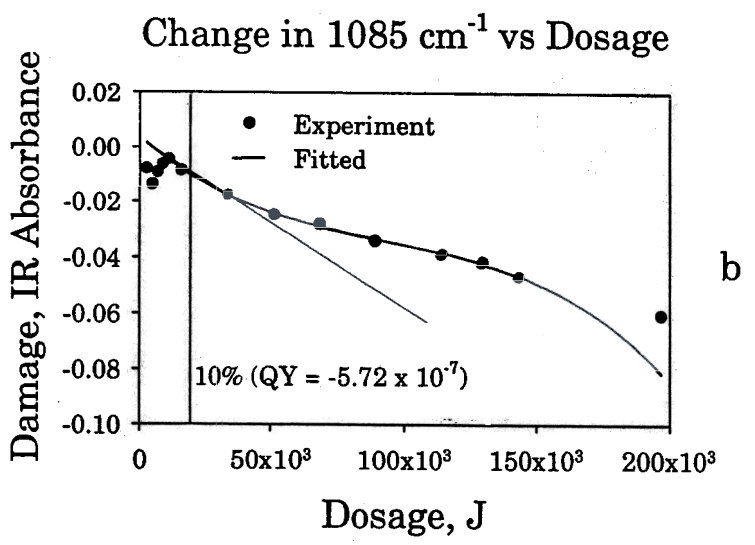

Figure 9. Experimental and fitting FTIR degradation data as a function of dosage for 1670 cm^{-1} and 1085 cm^{-1} bands. The initial slopes of these curves are used for obtaining the apparent spectral quantum yield.

imprecision in the measurements of very small changes at early exposures. Nevertheless, the polynomial function appears to fit most of the data well. Differentiating the polynomial gives the apparent quantum yield at a given dosage. Since the damage/dosage relationship is not linear, the apparent spectral quantum yield falls off with dosage, presumably due to increasing shielding of the coating by degradation products and to the consumption of weak links in the material.

Figure 10 presents typical apparent spectral quantum yield curves for the oxidation and crosslink chain scission of coatings exposed at 50 ° C and close to 0 %RH under full UV and the ten interference filters. The apparent quantum yield at 290 nm was the highest. In general, the apparent quantum yields in all UV exposure conditions for this coating were small, as is typical for solid polymers. Gupta et al. (21) have reported apparent quantum yield values (number of scissioned molecules per number of quanta absorbed by the polymer) in the range of 0.003-0.007 ± 0.002 for polycarbonates exposed to 300 nm to 400 nm wavelength radiation at temperatures 0° C and 55° C and at RH between 0 % and 100 %; whereas the apparent quantum yield of the same material irradiated in solution has been reported to be 0.18 (22). Dan and Guillet (23) observed that quantum yield of the chain scission in glassy polymers increases rapidly to the value obtained for the same polymer in solution as the temperature is increased to a temperature above the glass transition temperature.

Estimates of the total effective dosage and apparent spectral quantum yield were found to be very sensitive to a number of experimental variables, including the initial UV-visible absorbance of the coatings, formation of coating degradation products, anomalies in the spectral UV absorption of the substrate, and UV-visible and FTIR measurement errors. The effects of these variables on the dosage and spectral apparent quantum yield are reported in Reference 24. Protocols have been developed and experimental errors had been essentially eliminated through careful and frequent re-calibration of the UV-visible spectrophotometer using NIST's Standard UV-visible spectrometer transmittance density filters and polystyrene films to monitor the performance of the FTIR spectrometer before taking the spectra of any samples.

Conclusions

In this paper, a total effective dosage model has been presented that may have potential for linking field and laboratory photodegradation results for polymeric materials. An experimental apparatus and the experimental protocols for estimating the model coefficients have also been described.

The total effective dosage model has a basis in the principles of photochemistry and has had extensive application in the biological community. The primary inputs into the model are dose, dosage and material damage. Given this input, the apparent spectral quantum yield and the total effective dosage for a study material can be estimated.

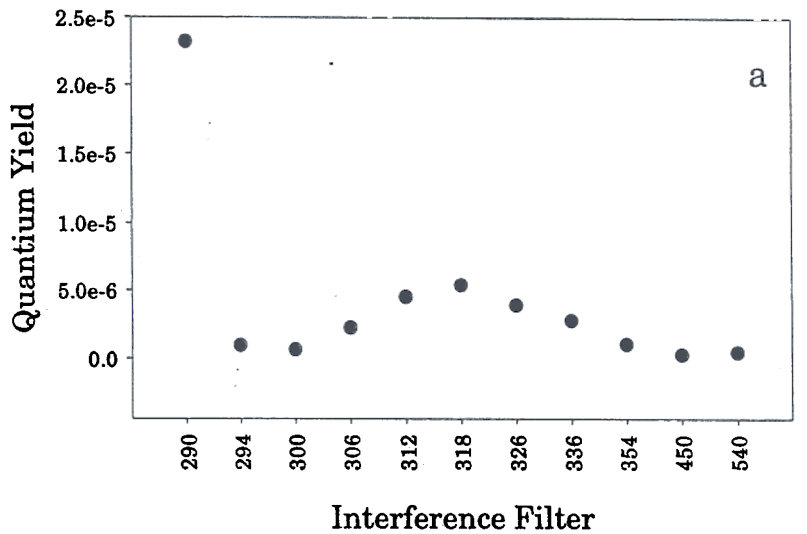

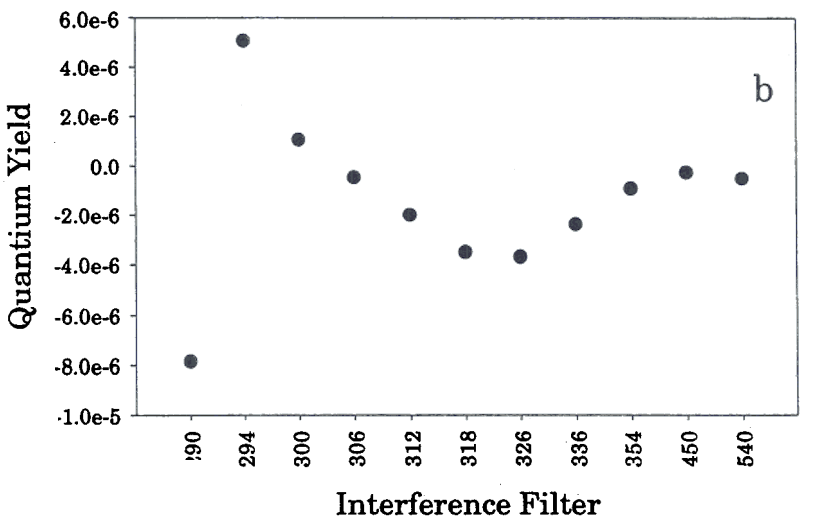

Figure 10. Quantum yields of the oxidation (a) and crosslink chain scission (b) of an acrylic melamine coating exposed to 50° C and close to 0% RH for full UV and 10 different wavelengths.

The exposure apparatus was built so that the primary exposure factors could be independently and accurately controlled and monitored within very tight bounds over both time and space. These factors include spectral UV radiation, temperature, and RH. Collimated UV radiation was produced by two 1000 W xenon arc solar simulators. Narrow band interference filters were used to segment the xenon arc spectrum into narrow bandwidths. Spectral damage to the coating was measured using Fourier transform infrared spectroscopy. Damage to the coating was attributed to hydrolysis, photolysis, and moisture-enhanced photolysis.

Experiments were conducted on the model coating covered a wide range of temperature and RH exposure conditions. A full 4x4 factorial experiment was conducted at four temperatures (30° C, 40° C, 50° C and 60° C) and four relative humidities (20 %, 40%, 70 %, and 90 %) and at each of twelve spectral wavebands. An extra experiment was conducted at 50° C and 0 % RH.

It was quickly determined that estimates of the total effective dosage and apparent spectral quantum yield were sensitive to a number of experimental variables including the formation of coating degradation products and UV-visible and FTIR measurement errors. To improve the precision of the measurements, both the UV-visible and the FTIR spectrometers were recalibrated during every inspection period. The spectral data was input into a computer program to estimate the dosage, the apparent spectral quantum yield, and the total effective dosage. This program provided near real-time updating of the total effective dosage model parameters by combining data from the current inspection period with historical data stored in the computer from previous inspections.

The total effective dosage model appears to be a good model for linking field and laboratory exposure results because the exposure apparatus built for this experiment greatly reduces temporal and spatial variations in the intensity of the three primary weathering factors – spectral ultraviolet radiation, temperature and relative humidity--it also allows separation of these effects. It was also shown that the experimental protocol for measuring or estimating the parameters of the total effective dosage model could be automated and that the outcome of these experiments for the study acrylic melamine coating are consistent with published results.

Acknowledgements:

The research reported here is part of a government/industry/university consortium on Service Life Prediction at NIST. Companies involved in this consortium include AKZO Nobel, ATOFINA, Atlas Electric Devices Inc., Dow Chemical, Dupont Automotives, Duron Inc., Eastman Chemicals, Millennium Inorganic Chemicals, PPG, and Sherwin Williams Co. Federal Highway Administration and Wright Patterson AFB provided additional funds for this research.

References

A.L. Norins, in F. Urbach (Ed.), The Biological Effects of Ultraviolet Radiation, Pergamon Press, N.Y., 1969, p. 605.

2. R. Setlow, Advanced Biological and Medical Physiology 5: 37 (1957).

R.M. Sayre, R.L Olson, and M.A. Everett, M.A, Journal of Investigative Dermatology 46: 240 (1966).

W.J.Clapson and J.A. Schaeffer, J.A., Journal of Industrial and Chemical Engineering, 26(9): 956 (1934).

5. G.Z. Zerlaut and M. L. Ellinger, J. Oil Colour Chem. Ass., 64, 387(1981)

6. G.A. Zerlaut, Accelerated and Outdoor Durability Testing of Organic Materials, W. D. Ketola and D. Grossman (Eds.), ASTM STP 1202, American Society for Testing and Materials, Philadelphia, PA, 1993, p. 3.

7. D.M. Grossman, Accelerated and Outdoor Durability Testing of Organic Materials, W. D. Ketola and D. Grossman (Eds.), ASTM STP 1202, American Society for Testing and Materials, Philadelphia, PA, 1993, p. 68.

8. D.R. Bauer, J.L. Gerlock, and D.F. Mielewski, Polym. Deg. Stab, 36,9 (1992).

9. D. Bauer and D.F. Mielewski, Polym. Deg. Stab., 40, 349 (1993).

10. J. D. Rancourt, Optical thin Films, User's Handbook, McGraw-Hill, NY, 1987, Chapter 6, p. 183.

11 J.W. Martin, E. Byrd, E. Embree, and T. Nguyen, A Collimated, Spectral Ultraviolet Radiation, Temperature, and Relative Humidity Controlled Exposure Chamber, in review.

12. K. Klein and B. Goldberg, Proc. Int. Solar Energy Soc. Conference, 1978, Vol. 1, p. 400.

13. G. Kampf, K. Sommer, and Zirngiebl, Prog. Org. Coat., 19, 69 (1991).

14. B. Dickens and E. Byrd, to be published as a NIST technical note.

15. D. R. Bauer and R.A. Dickie, J.Appl. Polym. Sci., 18, 2014 (1980).

16. P.J.Larkin, M.P. Makowski, and N.B. Colthup, Vibrational Spectroscopy 17(1998) 53.

17. D.R. Bauer, J. Appl. Polym. Sci., 27, 3651 (1982).

18. T. Nguyen, J. Martin, E. Byrd, and E. Embree, submitted for publication in the Journal of Coatings Technology.

19. J. Lemaire and N. Siampiringue, Service Life Prediction of Coatings and Materials, J. Martin, L. Floyd, D. Bauer, (Eds.), ACS Symposium Series 722, American Chemical Society, 1998, p. 246.

20. N.B. Colthup, L.H. Daly, and S.E. Wiberley, Introduction to Infrared and Raman Spectroscopy, 3 rd Ed., Academic Press, N.Y., 1990, p. 439.

21. A. Gupta, A. Rembaum, and J. Moacanin, Macromolecules, 11, 1285 (1978).

22. A. Gupta, A. R.Liang, J. Moacanin, R. Goldbeck, and D. Kliger, Macromolecules, 13, 262 (1980).

23. E. Dan and J.E. Guillet, Macromolecules, 6, 230 (1973).

24. J. Martin, T. Nguyen, E. Byrd, B. Dickens, and E. Embree, submitted for publication in Polymer Degradation and Stability.